INVENTORY OF SUPPLEMENTARY MATERIALS

Figure S1, related to Figure 1. Effects of SLAIN2 and ch-TOG depletion on MT dynamics.

Figure S2, related to Figure 1. Effects of SLAIN2 and ch-TOG depletion on cell morphology and migration in soft 3D matrices.

Figure S3, related to Figure 6. Effects of low doses of vinblastine and paclitaxel on MT dynamics, +TIP localization, cell morphology and migration in 2D, and invasive pseudopod maintenance and focal adhesions in 3D.

Figure S4, related to Figure 7. SLAIN2 requirement for metastatic outgrowth in mammary tumor and simulation of MT force-velocity dependence.

Movie S1, related to Figures 1 and S1. MT catastrophe induction by SLAIN2 depletion in 2D and 3D cultures.

Movie S2, related to Figures 1 and S1. 2D and 3D motility of SLAIN2-depleted cells.

Movie S3, related to Figure 2. Rab6A vesicle dynamics in invasive pseudopods of SLAIN2-depleted cells.

Movie S4, related to Figure 3. MT growth persistence at the tips of invasive pseudopods.

Movie S5, related to Figure 3. MT growth persistence and compression at the tip of invasive pseudopods.

Movie S6, related to Figure 4. Rescue of MT growth persistence by rapalog-induced recruitment of SLAIN2-N to MT plus ends.

Movie S7, related to Figure 5. MT catastrophes at the tips of invasive pseudopods induced by SLAIN2 or CLASP1 depletion.

Movie S8, related to Figures 6 and S3. MT catastrophe induction by low doses of MTAs in 2D and 3D cultures.

Movie S9, related to Figure 6. Loss of maintenance and elongation, but persistence of pseudopod initiation in low-dose MTA treated cells grown in soft 3D matrices.

Movie S10, related to Figure S3. Dynamics of MT plus ends, focal adhesions and Rab6A vesicles in soft 3D matrices during low-dose MTA treatment.

Supplementary Experimental Procedures

Supplementary References

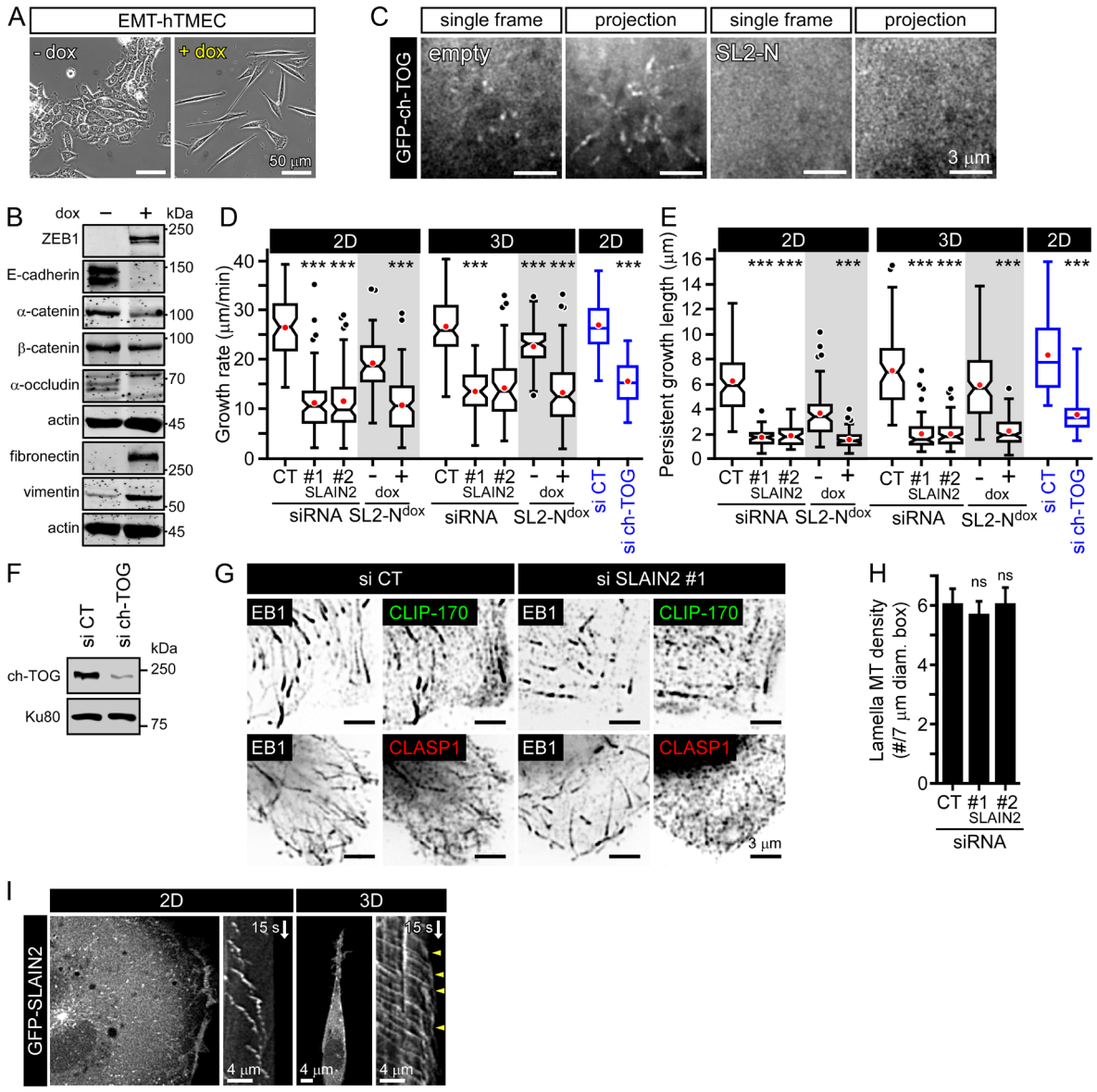
A
EMT-hTMEC
- dox
+ dox
50 µm
C
single frame
projection
single frame
projection
GFP-ch-TOG
empty
SL2-N
3 µm
B
dox – +
kDa
ZEB1
E-cadherin
α-catenin
β-catenin
α-occludin
actin
fibronectin
vimentin
actin
250
150
100
100
70
45
250
50
45
D
2D
3D
2D
Growth rate (µm/min)
CT #1 #2 - +
SLAIN2 dox
siRNA SL2-N^dox
si CT
si ch-TOG
E
Persistent growth length (µm)
F
si CT
si ch-TOG
kDa
ch-TOG
Ku80
250
75
G
si CT
si SLAIN2 #1
EB1
CLIP-170
CLASP1
3 µm
H
Lamella MT density (#/7 µm diam. box)
ns
CT #1 #2
SLAIN2
siRNA
I
2D
3D
GFP-SLAIN2
15 s
4 µm

Figure S1, related to Figure 1. Effects of SLAIN2 and ch-TOG depletion on MT dynamics.

A. Phase contrast images of non-tumor human mammary epithelial cells (hTMEC) converted into mesenchymal cells by doxycycline-induced (dox, 4 days) expression of ZEB1 (EMT-hTMEC).

B. Western blot analysis of epithelial (E-cadherin, α- and β-catenin, α-occludin) and mesenchymal markers (fibronectin, vimentin) in cells shown in (A).

C. Single frames and maximum intensity projections of GFP-ch-TOG live fluorescence image series acquired at 2 frames per second for 1 minute in HT-1080 cells co-transfected with either empty TagRFP or TagRFP-SL2-N vector. Ch-TOG comets are visible in control but not in TagRFP-SL2-N transfected cells.

D, E. MT growth rate (D) and persistent growth length (E) in MDA-MB-231 cells depleted of SLAIN2 by two independent siRNAs (#1 and #2), expressing a doxycycline-inducinble (dox) construct for the TagRFP-T-tagged dominant negative SLAIN2 mutant (SL2-N), or depleted of ch-TOG using siRNA. Cells were grown on 2D or in 3D matrix, as indicated. Box plots indicate the 25th percentile (bottom boundary), median (middle line), mean (red dots), 75th percentile (top boundary), nearest observations within 1.5 times the interquartile range (whiskers), 95% confidence interval of the median (notches) and outliers (black dots).

F. Western blot analysis of siRNA-mediated ch-TOG depletion in MDA-MB-231 cells.

G. Analysis of +TIP localization in SLAIN2-depleted MDA-MB-231 cells by immunofluorescence staining of EB1, CLIP-170 and CLASP1.

H. MT density in the lamella of SLAIN2-depleted MDA-MB-231 cells grown in 2D.

I. Live fluorescence images and kymographs of GFP-SLAIN2 in HT-1080 cells grown on collagen I-based stiff 2D or in 3D soft matrices. Arrowheads, MT growth persistence at the cell edge.

Bar plots are presented as mean ±SEM. In all plots, ns, no significant difference with control; ***, $P<0.001$, Mann-Whitney U test.

See also Movie S1.

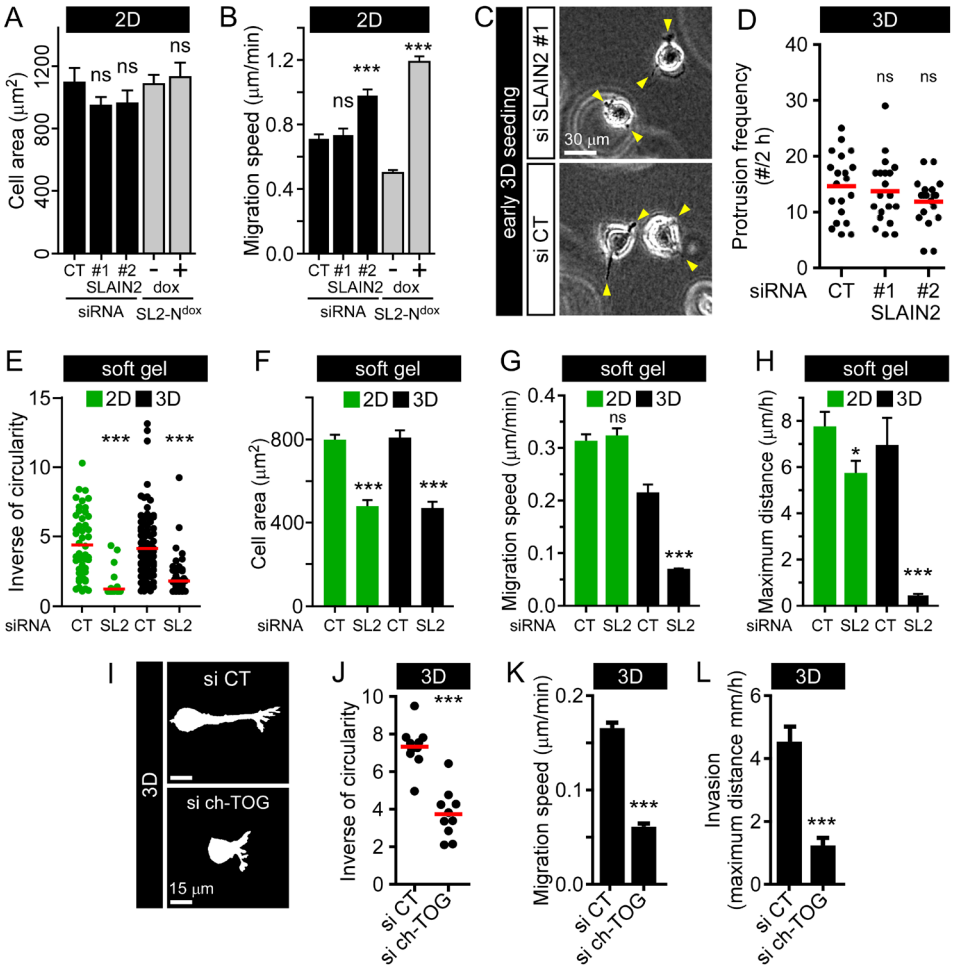
A
2D
Cell area (µm²)
ns
CT #1 #2 - +
SLAIN2 dox
siRNA SL2-N^dox
B
2D
Migration speed (µm/min)
***
ns
C
early 3D seeding
si SLAIN2 #1
si CT
30 µm
D
3D
Protrusion frequency (#/2 h)
siRNA CT #1 #2
SLAIN2
E
soft gel
2D 3D
Inverse of circularity
F
soft gel
Cell area (µm²)
G
soft gel
Migration speed (µm/min)
H
soft gel
Maximum distance (µm/h)
I
3D
si CT
si ch-TOG
15 µm
J
3D
Inverse of circularity
si CT
si ch-TOG
K
3D
Migration speed (µm/min)
L
3D
Invasion (maximum distance mm/h)

Figure S2, related to Figure 1. Effects of SLAIN2 and ch-TOG depletion on cell morphology and migration in soft 3D matrices.

A, B. Cell spreading (A) and migration speed (B) in 2D cultures of SLAIN2-depleted MDA-MB-231 cells.

C, D. Phase contrast images (C) and analysis of protrusion frequency (D) in SLAIN2-depleted MDA-MB-231 cells embedded (3D) in collagen I-based soft matrix for 2 hours. Arrowheads, protrusions.

E-H. Cell elongation (E), cell area (F), migration speed (G) and net displacement (H) of SLAIN2-depleted MDA-MB-231 cells grown either on top (2D) or within (3D) a collagen I-based soft matrix.

I-L. Cell morphology masks (I) and the corresponding quantification (J), migration speed (K) and invasion (L) of ch-TOG depleted MDA-MB-231 cells blocked in interphase by a 2 day-treatment with 2 mM thymidine; cells were grown in 3D matrix.

Bar plots are presented as mean ±SEM; in scatter plots, red bar: mean. In all plots, ns, no significant difference with control; ***, $P<0.001$, Mann-Whitney U test.

See also Movies S2.

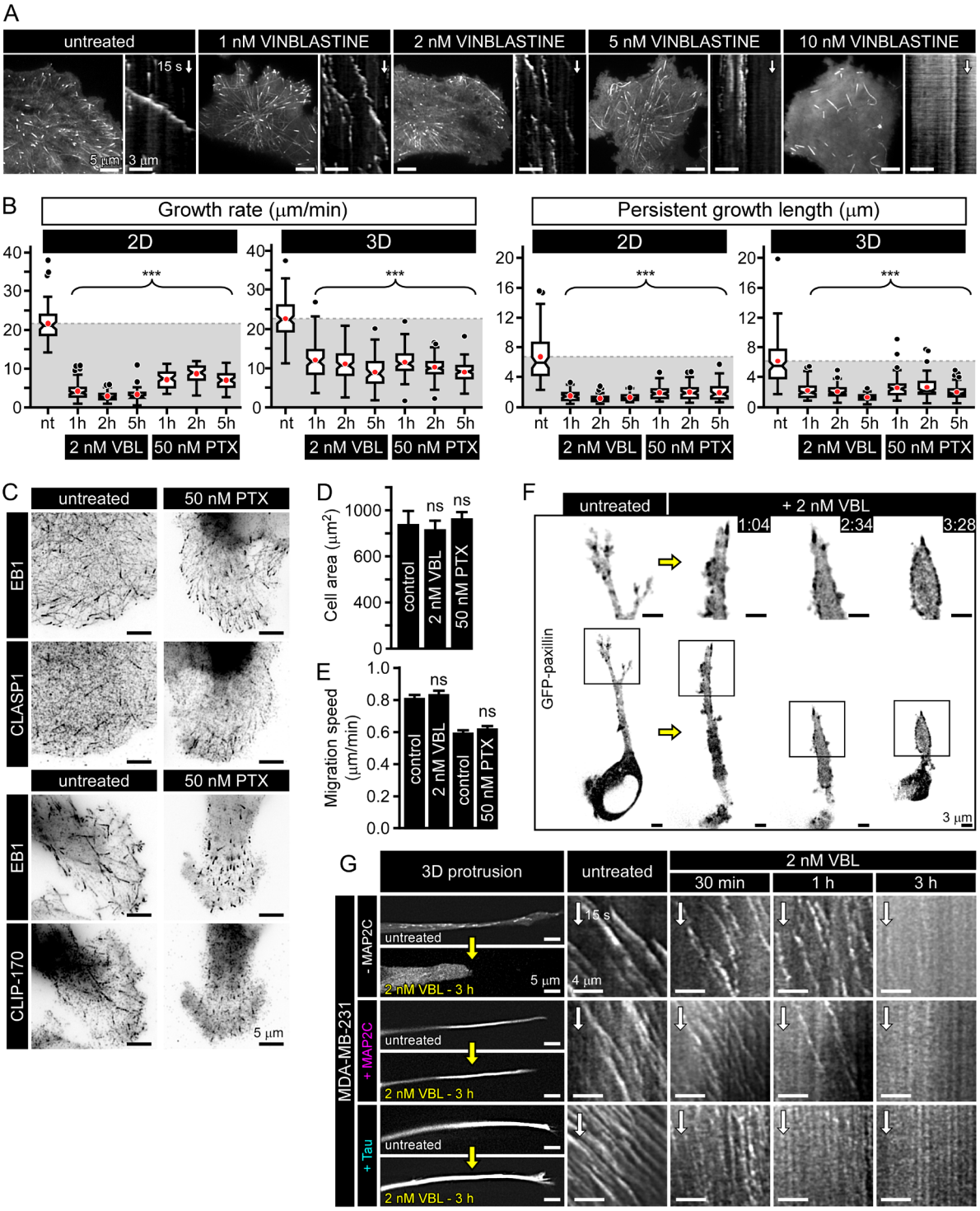
A
untreated
1 nM VINBLASTINE
2 nM VINBLASTINE
5 nM VINBLASTINE
10 nM VINBLASTINE
15 s
5 µm
3 µm
B
Growth rate (µm/min)
Persistent growth length (µm)
2D
3D
***
nt 1h 2h 5h 1h 2h 5h
2 nM VBL
50 nM PTX
C
untreated
50 nM PTX
EB1
CLASP1
CLIP-170
5 µm
D
Cell area (µm²)
ns
control
2 nM VBL
50 nM PTX
E
Migration speed (µm/min)
F
untreated
+ 2 nM VBL
1:04
2:34
3:28
GFP-paxillin
3 µm
G
3D protrusion
untreated
2 nM VBL
30 min
1 h
3 h
MDA-MB-231
- MAP2C
+ MAP2C
+ Tau
2 nM VBL - 3 h
15 s
4 µm
5 µm

Figure S3, related to Figure 6. Effects of low doses of vinblastine and paclitaxel on MT dynamics, +TIP localization, cell morphology and migration in 2D, and invasive pseudopod maintenance and focal adhesions in 3D.

A. Live fluorescence images of EB3-GFP and corresponding kymographs in cells treated with vinblastine as indicated.

B. MT dynamics parameters in 2D- or 3D-grown MDA-MB-231 cells treated as indicated (VBL, vinblastine; PTX, paclitaxel). Box plots are presented as in Fig. S1**.**

C. Immunofluorescence staining for EB1, CLASP1 and CLIP-170 in cells treated as indicated.

D, E. Cell spreading (C) and migration speed (D) in 2D-grown cells treated as indicated. Error bars, SEM.

F. Focal adhesions in invasive pseudopods visualized by confocal fluorescence imaging of GFP-paxillin in 3D grown cells treated as indicated (time, h:min).

G. Effect of MAP2C and Tau expression on invasive pseudopod maintenance when MT growth persistence is attenuated. Kymographs show EB3-GFP dynamics in cells treated as indicated. Panels on the right show invasive pseudopods before and after treatment; in +MAP2C and +Tau conditions, images illustrate mCherry-MAP2C and mCherry-Tau fluorescence, respectively.

See also Movies S8 and S10.

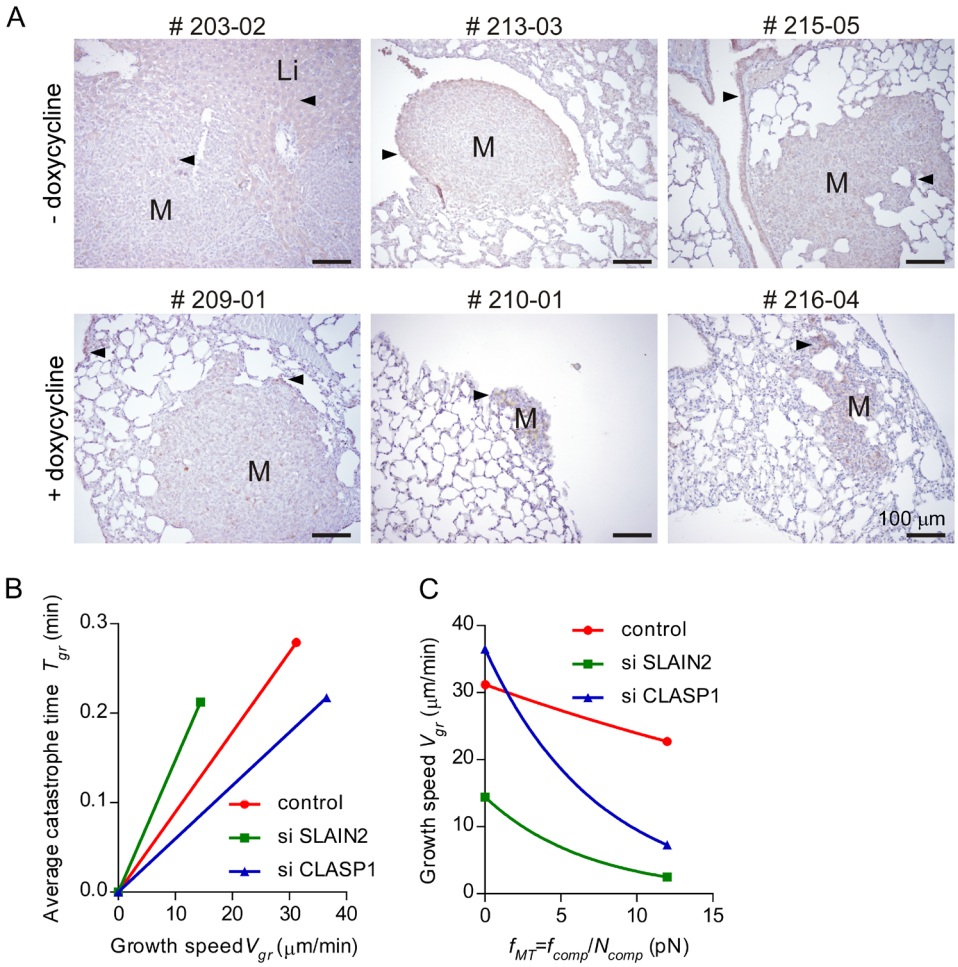
A
203-02
213-03
215-05
- doxycycline
Li
M
M
M
209-01
210-01
216-04
+ doxycycline
M
M
M
100 µm
B
Average catastrophe time T_{gr} (min)
0.3
0.2
0.1
0.0
0
10
20
30
40
Growth speed V_{gr} (µm/min)
control
si SLAIN2
si CLASP1
C
Growth speed V_{gr} (µm/min)
40
30
20
10
0
0
5
10
15
$f_{MT}=f_{comp}/N_{comp}$ (pN)
control
si SLAIN2
si CLASP1

Figure S4, related to Figure 7. SLAIN2 requirement for metastatic outgrowth in mammary tumor and simulation of MT force-velocity dependence.

A. Immunohistochemical staining for TagRFP in metastases from mice orthotopically transplanted with luciferase-expressing MDA-MB-231 cells carrying a doxycycline-controlled SL2-N expression cassette. Shown are lung and liver metastases from control mice (mice #203-02, 213-03, 215-05; top panels) or lung metastases from the 3 doxycycline-treated mice found positive for metastasis (mice # 209-01, 210-01, 216-04; bottom panels). M= metastasis; Li = liver tissue. Note the absence of specific TagRFP staining in the metastases from the doxycycline-treated mice. Black arrowheads depict non-specific staining in liver or lung epithelial cells. Bar represents 100 μm.

B. Linear dependence of the average catastrophe time on the growth rate for individual MTs used in the theoretical model. Experimental data are taken from Fig. 5G, N.

C. Fitting of force-velocity dependence for different conditions using two reference points: in the absence and in the presence of compressive force.

Movie S1, **related to Figures 1 and S1. MT catastrophe induction by SLAIN2 depletion in 2D and 3D cultures.** Top panels: confocal time-lapse imaging of EB3-GFP in MDA-MB-231 cells transfected with control siRNA (si CT) or SLAIN2-targeting siRNA (si SLAIN2 #2) and grown in 2D (left and center) or in 3D (right; green, EB3-GFP; red, Lifeact-mCherry). Bottom panels: confocal time-lapse imaging of EB3-GFP in MDA-MB-231 cells carrying a doxycycline-inducible expression construct for TagRFP-SLAIN2-N (RFP-SLAIN2-N), treated with vehicle (- dox) or doxycycline (+ dox). Cells were grown in 2D (left and center) or in 3D (right). Images were acquired at 0.5 s interval and are displayed at a 30 frames/s rate (accelerated 15 times).

Movie S2, related to Figures 1 and S1. 2D and 3D motility of SLAIN2-depleted cells. Phase contrast time-lapse imaging of control and SLAIN2-depleted MDA-MB-231 cells grown on collagen I-coated coverslips (Part 1; acquired at a 5 minute interval, displayed at 5 frames/s) or embedded in collagen I gel (Part 2; acquired at a 15 minute interval, displayed at 5 frames/s rate).

Movie S3, related to Figure 2. Rab6A vesicle dynamics in invasive pseudopods of SLAIN2-depleted cells. Confocal time-lapse imaging of GFP-Rab6A and TagRFP-T-CAAX in control and SLAIN2-depleted MDA-MB-231 cells grown in 3D. Images were acquired at a 0.5 s interval and are displayed at a 20 frames/s rate (accelerated 10 times).

Movie S4, related to Figure 3. MT growth persistence at the tips of invasive pseudopods. Confocal time-lapse imaging of EB3-GFP in Lifeact-mCherry-expressing MDA-MB-231 cells in 2D vs 3D cultures (Part 1) or at the tip of pseudopods grown in 3D (Part 2). Part 3 shows confocal imaging of EB3-GFP in human mammary epithelial cells carrying a

doxycycline-inducible cassette encoding ZEB1 (hTMEC-ZEB1^{dox}), treated with vehicle (- dox) or doxycycline (+ dox) for 6 days and grown in 3D for 3 days. Images were acquired at a 0.5 s interval and are displayed at a 30 frames/s rate (accelerated 15 times).

Movie S5, related to Figure 3. MT growth persistence and compression at the tip of invasive pseudopods. Confocal time-lapse imaging of β-tubulin-GFP in TagRFP-T-CAAX-labelled MDA-MB-231 cells grown in 3D. MT buckling occurs at the tip of elongating pseudopods during protrusion/retraction cycles. Images were acquired at a 2 s interval and are displayed at a 20 frames/s rate (accelerated 40 times).

Movie S6, related to Figure 4. Rescue of MT growth persistence by rapalog-induced recruitment of SLAIN2-N to MT plus ends. Confocal time-lapse imaging of FRB-GFP-SLAIN2-N and FKBP-TagRFP-SxIP before and after the addition of rapalog. Images were acquired at 0.5 s interval and are displayed at a 40 frames/s rate (accelerated 20 times).

Movie S7, related to Figure 5. MT catastrophes at the tips of invasive pseudopods induced by SLAIN2 or CLASP1 depletion. Confocal time-lapse imaging of EB3-GFP and TagRFP-T-CAAX in pseudopod tips of control, SLAIN2- and CLASP1-depleted MDA-MB-231 cells grown in 3D. Images were acquired at a 0.5 s interval and are displayed at a 40 frames/s rate (accelerated 20 times).

Movie S8, related to Figures 6 and S3. MT catastrophe induction by low doses of MTAs in 2D and 3D cultures. Confocal time-lapse imaging of EB3-GFP in 2D (upper panels) and 3D cultures (lower panels) of control (left), 2 nM vinblastine- (middle; 5 hours) or 50 nM

paclitaxel-treated MDA-MB-231 cells (right; 5 hours). Images were acquired at a 0.5 second interval and are displayed at a 30 frames/s rate (accelerated 15 times).

Movie S9, related to Figure 6. Loss of maintenance and elongation, but persistence of pseudopod initiation in low-dose MTA treated cells grown in soft 3D matrices. Phase contrast time-lapse imaging of 3D-grown MDA-MB-231 cells before (time in white) and after treatment with 2 nM vinblastine (left panels; time in yellow) or 50 nM of paclitaxel (right panels; time in orange). Images were acquired at a 5 minute interval and are displayed at a 10 frames/s rate (accelerated 3000 times).

Movie S10, related to Figure S3. Dynamics of MT plus ends, focal adhesions and Rab6A vesicles in soft 3D matrices during low-dose MTA treatment. Confocal time-lapse imaging of EB3-GFP and TagRFP-T-CAAX (Part 1; 0.5 s interval acquisition), GFP-paxillin (Part 2; 2 minute interval acquisition), and GFP-Rab6A and TagRFP-T-CAAX (Part 3; 0.5 s interval acquisition) in 3D-grown MDA-MB-231 cells before and after 2 nM vinblastine treatment as indicated. Images are displayed at a 20 frames/s rate.

Supplementary Experimental Procedures

Constructs and siRNAs

The pLVX-IRES-Hygro (pLVIH) and pLVX-IRES-Neo (pLVIN) vectors were constructed by cloning respectively the IRES-hygromycin resistance cassette from the pBabe-hTERT-Hygro plasmid (R. Weinberg, Whitehead Institute, Cambridge, USA; Addgene #1773) and the IRES-neomycin resistance cassette from the pQCXIN plasmid (Clontech) into the pLVX-IRES-Puro plasmid (pLVIP, Clontech). The EB3-GFP coding sequence (Stepanova et al., 2003) was inserted into pBABE-Zeo (R. Weinberg Whitehead Institute, USA; Addgene #1766) and pLVIH plasmids to generate the pBabe-Zeo-EB3-GFP and pLVIH-EB3-GFP plasmids. The Lifeact-mCherry coding sequence (Riedl et al., 2008) (a gift of M. Sixt, IST Austria, and R. Wedlich-Söldner, University of Münster, Germany) was inserted into pLNCX2 plasmid (Clontech) to generate the pLN-Lifeact-mCherry plasmid. The H2B-GFP coding sequence (pBOS-H2BGFP; BD Pahramingen) was cloned into pLNCX2 to generate the pLN-H2B-GFP plasmid. The CAAX coding sequence (Lansbergen et al., 2006) was cloned into the pEGFP-C2 plasmid (Clontech) to generate the pEGFP-C2-CAAX plasmid or into the pTagRFP-T-C1 plasmid (a gift of Y. Mimori-Kiyosue, RIKEN CDB, Kobe, Japan) to generate the TagRFP-T-CAAX cassette subsequently cloned into pLVIP resulting in the pLVIP-TagRFP-T-CAAX plasmid. The β-tubulin-GFP coding sequence (kindly provided by K. Jiang, Utrecht University, the Netherlands) was cloned into pLVIP to generate the pLVIP-β-tubulin-GFP plasmid. The Tet-responsive transactivator (rtTA2sM2) coding sequence from the pSIN-TRE-mSEAP-hPGK-rtTA2sM2 plasmid (pSIN-TRE-rtTA; a gift of I.Barde and D. Trono, EPFL, Switzerland) (Barde et al., 2006) was cloned into pLVIP to generate the rtTA2sM2-IRES-Puro cassette subsequently cloned into pSIN-TRE-rtTA resulting in the all-in-one pSIN-TRE-rtTA-IRES-Puro plasmid carrying a doxycycline-inducible expression cassette and a separate constitutive expression cassette for rtTA2sM2 and puromycin resistance. The human ZEB1

coding sequence from the pcDNA4hismaxCZEB1 plasmid (a gift of J. E. Mertz, McArdle Laboratory for Cancer Research, Madison, USA) (Ellis et al., 2010) was cloned into pLVX-Tight-Puro (Clontech) and pSIN-TRE-rtTA-IRES-Puro plasmids to generate the pLVX-TP-ZEB1 and pSIN-TRE-rIP-ZEB1 plasmids, respectively. The pEGFP-C1-SLAIN2 plasmid was previously described (van der Vaart et al., 2011) and the coding sequence of the human SLAIN2 protein N-terminus (SLAIN2-N, amino acids 1-267) (van der Vaart et al., 2011) was cloned into pTagRFP-T-C1 to generate the pTagRFP-T-SLAIN2-N plasmid. The resulting TagRFP-T-SLAIN2-N cassette was cloned into pSIN-TRE-rtTA-IRES-Puro and pQCXIN to generate the pSIN-TRE-rIP-RFP-SLAIN2-N and pQCXIN-RFP-SLAIN2-N plasmids, respectively. The Rho biosensor coding plasmid pLenti-RhoA2G is a gift of O. Pertz, University of Basel, Switzerland (Addgene plasmid # 40179). The Rac1 biosensor coding sequence from the pTriEX-His-Myc4-Rac1-biosensor plasmid (Moshfegh et al., 2014) was cloned into pLVIN to generate the pLVIN-Rac1-bs plasmid. The pC5V (Cerulean-5-Venus), pCerulean-C1 and pmVenus-C1 plasmids were purchased from Addgene (# 26394, S. Vogel; # 54604, M. Davidson and D. Piston; # 5465, M. Davidson). The GFP-Rab6A coding sequence (Grigoriev et al., 2007) was cloned into pQCXIN to generate the pQCXIN-GFP-Rab6A plasmid. The pQC-GFP-paxillin was previously described (Bouchet et al., 2011). The FRB and SLAIN2-N coding sequences from respectively the pC_4-R_HE (ARGENT^{TM}) and pTagRFP-T-SLAIN2-N plasmids were cloned into pEGFP-C2 plasmid, and the resulting FRB-GFP-SLAIN2-N cassette was subsequently cloned into pLVIP to generate the pLVIP-FRB-GFP-SLAIN2-N plasmid. The FKBP-TagRFP-T-MACF18LZ coding sequence (Honnappa et al., 2009) (a gift of P. Schätzle, Utrecht University, the Netherlands) was cloned into pLVIN to generate the pLVIN-FKBP-TagRFP-T-SxIP plasmid. The GFP-CLASP1α (Akhmanova et al., 2001) was cloned into pLVIH to generate the pLVIH-GFP-CLASP1 plasmid. The pmCherry-MAP2C and pmCherry-4R-Tau plasmids were a gift of C.

Hoogenraad, Utrecht University, the Netherlands. The pLVX-Tet-On Advanced plasmid and the lentiviral Lenti-X HTX Packaging vector mix were purchased from Clontech. The retroviral packaging vector pCL-Ampho was kindly provided by E. Bindels, Erasmus MC, The Netherlands. The lentiviral packaging vectors psPAX2 and pMD2.G were kindly provided by E. Soler, Erasmus MC, the Netherlands. The GFP-ch-TOG vector pBrain-GFP-ch-TOGKDP-shch-TOG simultaneously expressing an shRNA for depleting human ch-TOG and a GFP-tagged ch-TOG rescue construct was a gift of S. Royle (Warwick Medical School, UK) (Gutierrez-Caballero et al., 2015). Individual siRNAs targeting SLAIN2, ch-TOG, CLASP1, CLASP2 and CLIP-170, and luciferase targeting control siRNA were previously described (Lansbergen et al., 2006; Mimori-Kiyosue et al., 2005; van der Vaart et al., 2011). For experiments based on ch-TOG depletion, 2 mM thymidine was added one day after siRNA transfection and 2 days prior to imaging in order to block cells in interphase and avoid mitosis-related cell rounding. In ch-TOG- and CLASP-depleted 3D cultures, mitotic cells were excluded from morphology and migration analysis using H2B-GFP fluorescence imaging to monitor chromosome condensation.

Antibodies and cell culture reagents

The rat monoclonal antibody against tyrosinated α-tubulin (YL1/2) was purchased from Abcam. Mouse monoclonal antibodies against the following proteins were used: α-tubulin (DM1A), fibronectin (FN-3E2), vimentin (V9) and phospho-tyrosine (Sigma-Aldrich); E-cadherin (36/E-Cadherin), α-catenin (5/a-catenin), β-catenin (14/Beta-Catenin), α-occludin (19/Occludin), Ku80 (7/Ku80) and EB1 (BD Biosciences); actin (C4) (Merck-Millipore); Rho, Rac1 and Cdc42 (Cytoskeleton); GFP (Roche). We used rabbit polyclonal antibody against ZEB1 (Bethyl Laboratories), SLAIN1/2 (van der Vaart et al., 2011), ch-TOG (a gift from L. Cassimeris, Lehigh University), CLASP1 (Mimori-Kiyosue et al., 2005), CLIP-170

and CLASP2 (Akhmanova et al., 2001), EB3 (Stepanova et al., 2003) and TagRFP (Evrogen). Note that the anti-SLAIN1/2 antibody used here also recognizes SLAIN1, but the depletion of SLAIN2 alone was sufficient to strongly decrease the total SLAIN signal, indicating that SLAIN1, which is predominantly neuronal (van der Vaart et al., 2012), does not contribute significantly to the SLAIN2 pool in the investigated cells.

Alexa Fluor 405-, Alexa Fluor 488- and Alexa Fluor 594-conjugated goat antibodies against rat, rabbit and mouse were purchased from Life Technologies. For Western blotting, IRDye 800CW-conjugated goat antibody against rabbit IgG and IRDye 680LT-conjugated goat antibody against mouse IgG were purchased from Li-Cor Biosciences.

Rat tail collagen Type I (high concentration) for soft 3D culture was purchased from Corning and bovine dermis pepsin-extracted collagen I solution for stiff 2D culture was purchased from Advanced BioMatrix (PureCol). Stiffness of rat tail collagen I gels was defined based on previous publications using an identical preparation method, similar invasive cell lines and elastic modulus measurement (Heck et al., 2012; Wolf et al., 2013). Phenol red-free Matrigel was purchased from BD Biosciences. For collagenolysis assay, fluorescein conjugated DQ collagen (type I from bovine skin, Life Technologies) was prepared according to the manufacturer's instructions and mixed at a final concentration of 25 μg/ml with the gel preparation. Collagenolysis was observed by confocal imaging 2 days after seeding. DMEM, MEBM and supplement (human EGF, insulin, hydrocortisone, bovine pituitary extract, gentamicin and amphotericin-B) and trypsin neutralizing solution were purchased from Lonza. DMEM/F12 and RPMI 1640 were purchased from Life Technologies.

We used the following chemicals, reagents and drugs: Alexa Fluor 594- and Alexa Fluor 488-conjugated phalloidin and G418 (Geneticin) (Life Technologies); puromycin and hygromycin (InvivoGen); thymidine, vinblastine sulfate, ROCK1 inhibitor Y-27632, sodium borohydride ($NaBH_4$), DAPI, Triton X-100, Tween 20, bovine serum albumin (BSA), poly-

HEMA and doxycycline hydrochloride solution (Sigma-Aldrich); polybrene and Rac1 inhibitor NSC23766 (Merck-Millipore); paclitaxel and blebbistatin (Enzo Life Sciences); polyethyleneimine "Max" (MaxPEI) (Polysciences); latrunculin B (Santa Cruz Biotechnology); Rapalog (Clontech); Vectashield (Vector Laboratories); paraformaldehyde (16%) and glutaraldehyde (10%) (Electron Microscopy Sciences); poly-D-lysine (MP Biomedicals).

Click-iT EdU Cell Proliferation assay was purchased from Life Technologies, performed according to manufacturer's instructions and analyzed on 10-20 independent fields of view (~100-500 cells per condition). FuGENE6 Transfection Reagent (cDNA) was purchased from Roche. HiPerFect Transfection Reagent (siRNA) was purchased from Qiagen. Amaxa Cell Line Nucleofector Kit V was purchased from Lonza. Multi-well glass bottom and slide chambers were purchased from Thermo Scientific. Rac1/Cdc42 and Rho activation assay kits were purchased from Cytoskeleton and used according to the manufacturer's instructions in sparse cell cultures stimulated with fresh 10% FCS-containing medium 3 hours before lysis (n = 5-6 independent experiments); 800 μg of pre-cleared whole cell lysis were incubated with 15 μg of Rhotekin-RBD (Rho) or 10 μg of PAK-PBD (Rac1) beads and input was as indicated in Figure 3.

Transfection, lentiviral infection and cell line selection

Lentivirus packaging was performed by MaxPEI-based co-transfection of HEK293T cells with psPAX2, pMD2.G and the lentiviral vector of interest. In the case of non-self-inactivated vectors (pLVX-based vector, Clontech), the vector of interest was co-transfected with the Lenti-X HTX packaging mix. Retrovirus packaging was performed by co-transfection of HEK293T cells with pCL-Ampho vector with the retroviral vector of interest. Supernatant of packaging cells was harvested up to 72 hours after transfection, 0.45 μm-filtered and

incubated with a PEG 6000-based precipitation solution overnight at 4°C. After precipitation, virus was concentrated up to 100 times by centrifugation and dissolution in 1X phosphate buffered saline (PBS). Target cells were incubated for 4 hours in complete medium supplemented with 8 μg/ml polybrene before infection. Medium was replaced 24-48 hours after infection and eventual antibiotics for selection were added.

Clonal MDA-MB-231 stable lines expressing the following combinations of tagged proteins were established by infection using the plasmids and viruses described above, antibiotics selection (2 μg/ml puromycin; 500-750 μg/ml G418) and/or limiting dilution-based subcloning: Lifeact-mCherry, EB3-GFP, Lifeact-mCherry and EB3-GFP, H2B-GFP, TagRFP-T-CAAX and β-tubulin-GFP, doxycycline-inducible TagRFP-T-SLAIN2-N, TagRFP-T-CAAX and GFP-Rab6A', FRB-GFP-SLAIN2-N and FKBP-TagRFP-T-SxIP, and GFP-paxillin. Clonal HT-1080 stable lines expressing the following tagged proteins were established by infection using the plasmids and viruses described above, using antibiotics selection (2 μg/ml puromycin; 600 μg/ml G418) and/or limiting dilution-based subcloning: Rho biosensor, Rac1 biosensor and EB3-GFP. Clonal hTMECs stable lines expressing the following combinations of proteins were established by infection using the plasmids and viruses described above, antibiotics selection (0.5 μg/ml puromycin; 100-200 μg/ml G418) and/or limiting dilution-based subcloning: EB3-GFP, doxycycline-inducible ZEB1, EB3-GFP and doxycycline-inducible ZEB1, and doxycycline-inducible ZEB1 and constitutive TagRFP-T-SLAIN2-N. hTMEC clones carrying ZEB1-inducible expression (hTMEC-ZEB1^{dox}) were selected based on ZEB1 expression level analyzed by Western blotting and efficient and sustained EMT characterized by morphology and Western blotting-based analysis of epithelial and mesenchymal markers after 0.5-1 μg/ml doxycycline treatment.

Transient overexpression of Cerulean, mVenus, C5V, mCherry-MAP2C and GFP-CAAX, or mCherry-4R-Tau was achieved by FuGENE6-based transfection in HT-1080 cells

and Amaxa Cell Line Nucleofector Kit V-based nucleofection in MDA-MB-231 cells, 24-48 hours prior imaging and according to manufacturer instructions. Transfection of 5-10 nM siRNA in MDA-MB-231 and HT-1080 cells was performed using HiPerFect according to manufacturer's instructions.

Working solutions of vinblastine and paclitaxel were freshly prepared for each experiment and diluted in DMSO and complete medium. ROCK1 inhibitor Y-27632 was used at 10 μM, myosin II inhibitor blebbistatin was used at 50 μM, Rac1 inhibitor NSC23766 was used at 200 μM, latrunculin B was used at 10 μM and rapalog was used at 100 nM. Inhibitors were either added to the culture medium for short-term treatment and/or mixed with the gel for long treatment in 3D cultures.

Fluorescent staining, microscopy of fixed samples and analysis

For immunofluorescence staining of α-tubulin and F-actin in 2D cultures, cells were first extracted for 30 seconds at room temperature (RT) with 0.2 % Triton X-100 in cytoskeleton stabilizing buffer (CSB; 60 mM PIPES, 20 mM HEPES, 1 mM $MgCl_2$, 4 mM EGTA, 100 mg/ml sucrose), fixed in 2% PFA/0.1% glutaraldehyde in CSB for 10 minutes, permeabilized in 0.2% Triton X-100 for 15 minutes at RT, blocked in 1% BSA diluted in 1X PBS supplemented with 0.05% Tween 20. Samples were then sequentially incubated at RT with mouse monoclonal antibody against α-tubulin, Alexa Fluor 488-conjugated goat antibodies against mouse IgG, and 2 μg/ml DAPI/1:200 Alexa Fluor 594-conjugated phalloidin and after the final wash, dried and mounted in Vectashield. Cell area in 2D cultures was measured in 10-17 cells. Lamella MT density was performed using ImageJ in images of α-tubulin staining by manual counting, using a 7 μm-diameter region of interest (n=25, 5 cells). For immunofluorescence staining of focal adhesions, cells were fixed in 4% PFA for 15 minutes, permeabilized in 0.2% Triton X-100 for 5 minutes at RT, blocked in 1% BSA diluted in 1X

PBS supplemented with 0.05% Tween 20, sequentially incubated at RT with mouse monoclonal antibody against phospho-tyrosine, Alexa Fluor 488-conjugated goat antibodies against mouse IgG and Alexa Fluor 594-conjugated phalloidin. For quantification of focal adhesion in 3D, phospho-tyrosine clusters larger than 0.1 μm^2 were manually counted and measured using ImageJ (n=8 cells). For focal adhesion quantification in 2D, phospho-tyrosine clusters larger than 0.1 μm^2 were counted using particle analyzer in ImageJ (n=14 cells).

For immunofluorescence staining of α-tubulin and F-actin in 3D cultures, cells were incubated with 0.5% Triton X-100/0.1% glutaraldehyde CSB pre-extraction buffer at 37°C for 5 minutes, fixed in 0.3% glutaraldehyde diluted in 1X PBS for 10 minutes at RT, rinsed in 1X PBS, permeabilized for 30-45 minutes at RT in 0.5-0.7% Triton X-100 diluted in 1X PBS and blocked 30 minutes at RT in 1% BSA diluted in 1X IF wash solution (10X stock; 38.00 g NaCl 9.38 g Na_2HPO_4, 2.07 g NaH_2PO_4, 2.5 g NaN_3, 10 ml Triton X-100, 2.5 ml Tween-20, 500 ml MilliQ water, pH 7.4). Glutaraldehyde was quenched 1-3 times for 5 minutes using 2.5 mg/ml $NaBH_4$ diluted in permeabilizing solution. Incubation with the rat monoclonal antibody against tyrosinated α-tubulin was performed for 3 hours at RT or overnight at 4°C. Alternatively, incubation with mouse monoclonal antibodies against α-tubulin was used and 2% PFA/0.1% glutaraldehyde was used for fixation. Secondary antibody, DAPI, and Alexa Fluor 488 or 594-conjugated phalloidin incubations were performed as described above. Multi-well supports were dismounted, 3D gel plugs were dried at RT, covered with Vectashield and coverslip, incubated overnight at RT and the resulting sample was sealed with nail polish.

2D Samples were imaged using widefield fluorescence illumination on a Nikon Eclipse 80i upright microscope equipped with a CoolSNAP HQ^2 CCD camera (Photometrics), an Intensilight C-HGFI precentered fiber illuminator (Nikon), ET-DAPI, ET-EGFP and ET-mCherry filters (Chroma), controlled by Nikon NIS Br software and using a Plan Apo VC

100x NA 1.4 oil, Plan Apo VC 60x NA 1.4 oil or a Plan Fluor 20x MI NA 0.75 oil objective (Nikon). For presentation, images were adjusted for brightness and processed by Gaussian blur and Unsharp mask filter using ImageJ 1.47v (NIH). For cell area measurement, Alexa Fluor 594-conjugated phalloidin images were processed for threshold to reveal the cell edge, and the binary cell mask obtained was selected and measured using ImageJ 1.47v.

3D samples were imaged by confocal fluorescence microscopy on a Nikon Eclipse Ti microscope equipped with a perfect focus system (PFS, Nikon), a spinning disk-based confocal scanner unit (CSU-X1-A1, Yokogawa), an Evolve 512 EMCCD camera (Photometrics) attached to a 2.0X intermediate lens (Edmund Optics), a super high pressure mercury lamp (C-SHG1, Nikon), a Roper Scientific custom-made set of Stradus 405 nm (100 mW, Vortran), Calypso 491 nm (100 mW, Cobolt) and Jive 561 nm (100 mW, Cobolt) lasers, a set of ET-BFP2, ET-EGFP, ET-mCherry and ET-EGFP-mCherry filters (Chroma) for widefield fluorescence observation, a set of ET460/50m, ET525/50m or ET535/30m (green), ET630/75m (red) and ET-EGFP/mCherry filters (Chroma) for spinning disk-based confocal imaging and a motorized stage MS-2000-XYZ with Piezo Top Plate (ASI). The microscope setup was controlled by MetaMorph 7.7.11.0. Images were acquired using Plan Fluor 10x NA 0.3 air, Plan Fluor 20x MI NA 0.75 oil, Plan Apochromat λ 60x NA 1.4 oil and Plan Apo VC 60x NA 1.4 oil objectives.

Z-series images of fluorescent staining of α-tubulin, F-actin and DQ collagen in 3D cultures were acquired using 0.2 µm-step confocal-based scan (50-145 z-planes) and were presented as maximum projections adjusted for brightness and eventually processed by Gaussian blur and unsharp mask filter using ImageJ 1.47v or deconvolved using Huygens Software 4.4.0p9 (SVI). Images of DQ collagen with Lifeact-mCherry or TagRFP-CAAX were acquired similarly and single planes are displayed. Collagen degradation index was calculated using DQ collagen fluorescence images processed by Gaussian blur and

background subtraction using ImageJ. It represents the ratio of pixel intensity sum in the first 5 μm away from the cell body to the same value in the next 5 μm recorded by 10 pixel-wide selection lines (Plot profile)(n=15, 5 cells).

Cell circularity and area in 3D or on-top cultures was measured on maximum projection of z-series images when the z distribution of the cell body did not span the average z dimension of a completely rounded cell (approximately 20 μm) to limit z-related bias in morphology analysis (n = 10-35 cells). Binary cell mask obtained after thresholding was analyzed using ImageJ 1.47v for circularity.

Live cell imaging and analysis

Kymograph-based analysis of MT plus end dynamics was carried out using cells stably expressing EB3-GFP as previously described (van der Vaart et al., 2011) using a 1 μm cut-off for a growth event and Kymograph ImageJ plugin (A. Seitz, EPFL, Switzerland, http://biop.epfl.ch/TOOL_KYMOGRAPH.html). For the dataset presented, 44-176 growth events were analyzed in 5-20 cells. For presentation, images were adjusted for brightness and processed by Gaussian blur and unsharp mask filter using ImageJ 1.47v. For the analysis of growing MT plus end residence within 5 μm from the cell edge, 2-channel kymographs (EB3-GFP/ Lifeact-mCherry or TagRFP-T-CAAX,) were used. Only the MT growth events starting and finishing within the time of the recording and displaying a velocity ranging from 2-fold slower than average to ~0 μm/min (stationary comet) were classified as residence events and subsequently quantified for duration (n = 124-309, 11-29 cells). For β-tubulin-GFP/TagRFP-T-CAAX imaging and MT buckling analysis, images were acquired by confocal fluorescence at one optimal z-plane, adjusted for brightness, processed by Gaussian blur, background subtraction and unsharp mask filter using ImageJ 1.47v.

Load-bearing capacity of MTs at the cell cortex in the absence of F-actin was analyzed in two ways. First, adherent cells were treated with latrunculin B followed by immediate simultaneous fluorescence imaging of EB3-GFP and TagRFP-T-CAAX on the spinning disk-based confocal imaging station described above (n = 24-32 cells). To build distributions of EB3-GFP comet velocity during protrusion formation, we used kymograph-based analysis. Two-channel kymographs (EB3-GFP, TagRFP-T-CAAX) were built along a line traced at the estimated average position of the protrusion using the ImageJ plugin KymoResliceWide (https://github.com/ekatrukha/KymoResliceWide). Only EB3-GFP comets, which were localized to protrusion tips and the position of which correlated with the elongation of the protrusion were analyzed. Individual growth events were manually traced using segmented line tool of ImageJ. The resulting coordinates (x, t) were imported into Matlab and analyzed using a custom written script. Instantaneous velocity extracted from the slope of each segment within a tracing was assigned to the corresponding protrusion length. All growth episodes were inversely ranked with the end position being assigned to the zero coordinate and the start position assigned to the maximum protrusion length value. Corresponding MT growth rate as a function of its relative position to the tip of the protrusion at maximum length was sampled at 0.1 μm intervals and presented as a multiple event average per bin. To facilitate the comparison between control and SLAIN2-depleted cells, data points from protrusion length >3 μm were excluded from analysis. Alternatively, MT ability to push cortical membrane in the absence of F-actin was analyzed by counting (n = 15 cells) and measuring (n = 29-145) cortical protrusions (length cut-off, 2.5 μm) formed in cells treated for 15 minutes with latrunculin B and cultured on a poly-HEMA-treated non-adherent support. Measurements were performed on masks obtained from maximum projection of z-series of 1 μm-step confocal fluorescence images of TagRFP-CAAX expressing cells.

FRET-based analysis of Rho and Rac1 activity was performed on clonal HT-1080 cells lines described above and stably expressing the previously described Rho single chain biosensor (Fritz et al., 2013) or Rac1 single chain biosensor (Moshfegh et al., 2014). Fluorescence imaging of Rho and Rac1 biosensors was performed on the spinning disk-based confocal imaging station described above implemented with a ET-ECFP/EYFP filter (Chroma), a Stradus 445 nm (80mW, Vortran) laser for excitation of mTFP1 (Rho biosensor) and mCerulean (Rac1 biosensor), a dichroic filter T505lpxr equipping the DV2 device for simultaneous blue and yellow fluorescence imaging and a Di01-T442/514/647 emission filter (Semrock). Biosensor probe distribution was monitored by mTFP1/mCerulean fluorescence imaging upon 445 nm excitation, compared to mVenus fluorescence upon 445 nm excitation (FRET) and used to detect eventual aggregation/sequestration-related artefacts. To minimize cell motion-related artefacts, mTFP1/mCerulean and mVenus emission upon 445nm excitation were recorded simultaneously using the DV2 device. Manual alignment of the DV2 mirrors was performed to reduce as much as possible misalignment-related artefacts in the FRET/mTFP1 or mCerulean fluorescence ratio calculation and spatial distribution. When necessary, further adjustment was performed using split images and ratiometric result obtained from a custom written ImageJ macro. The standards Cerulean (pmCerulean-C1), mVenus (pmVenus-C1) and positive control C5V (pC5V) (Koushik et al., 2006) were imaged with the same setup in transiently transfected HT-1080 cells. Using thresholding on the FRET image, a cell mask was determined and applied to the 32-bit FRET/mTFP1 or mCerulean ratiometric image to measure mean ratio value within each cell. For presentation purposes, the 32-bit ratiometric image was submitted to Gaussian blur, a 16 color-lookup table was applied and a 8-bit color calibration bar is displayed. For 2D cultures, single plane confocal images were acquired at the ventral cell cortex (n = 40 cells). In 3D cultures, single plane confocal images were acquired at position allowing maximal measurement of Rho (n = 10) or Rac1 (n

= 17) activity over the cell body including pseudopods and later processed using thresholding to exclude both outside of the cell and nucleus from the analysis. 2D and 3D cultures were respectively imaged using a Plan Fluor 40x NA 1.3 and Apo LWD λS 40x NA 1.15 with a supplementary image series using an extra 1.5x magnification before projection on the camera chip for 3D protrusion tip analysis.

Rab6A-GFP vesicle dynamics within 5 μm of the pseudopod tip was analyzed on kymographs from 3D confocal imaging (n = 12-13 cells; 112-162 moving towards the tip; 50-73 vesicles moving towards the cell body; 121-128 immobile vesicles). GFP-paxillin images were used for focal adhesion counting at the tip of live cells grown in 3D (n=8, 4 cells).

Phase contrast and wide field fluorescence live cell imaging were performed on a Nikon Ti equipped with a perfect focus system (PFS, Nikon), a super high pressure mercury lamp (C-SHG1, Nikon), Lambda SC Smart Shutter controllers (Sutter), a Plan Apochromat DM 20x NA 0.75 (Ph2) or a Plan Fluor DLL 10x NA 0.3 (Ph1), a ET-mCherry filter (Chroma), a CoolSNAP HQ^2 CCD camera (Photometrics), a motorized stage MS-2000-XYZ with Piezo Top Plate (ASI) and a stage top incubator INUG2E-ZILCSD-DV (Tokai Hit) for 37°C/5% CO2 incubation. The microscope setup was controlled by the open source microscopy software Micro-Manager. Processing with Gaussian blur and Unsharp mask filter using ImageJ 1.47v was used for presentation. Red fluorescent images were subjected to background subtraction and adjusted for brightness before the overlay with phase contrast images. Alternatively, phase contrast and widefield fluorescence live cell imaging were performed using the BioStation CT (Nikon) equipped with a 2/3-inch cooled CCD camera, a high-intensity red LED for phase contrast imaging, and a 460-490 nm LED and a GFP-3035B filter block (Semrock) for green fluorescence imaging. Cell migration speed and distance from starting point were analyzed in 5 minute interval/1.5 hour long (2D) or 15 minute interval/20 hours long (3D; on-top) time-lapse recordings (n = 21-114 cells) using the

MTtrackJ plugin v1.5.0 in ImageJ 1.47v. Inverse of circularity and cell area in soft 3D vs soft 2D matrices (n = 48-108), CLASP1-overexpressing vs control cells (n=12) and rapalog-based rescue (n = 37-44) were analyzed on phase contrast images. Protrusion frequency in SLAIN2-depleted cells (Fig. S2D) was analyzed by manual counting using phase contrast time-lapse recording of 3D cultures started one hour after 3D seeding and performed for 2 hours (n=19-20 cells).

Immunohistochemistry in mouse tissues

Tissues were isolated and fixed in 4% formalin. Tissues were cut into 4 μm sections, dehydrated, and stained with hematoxylin and eosin. For immunohistochemical stainings, fixed sections were rehydrated and incubated with rabbit anti-TagRFP antibody (1:200). Endogenous peroxidases were blocked with 3% H_2O_2 followed by incubation with HRP-conjugated secondary anti-rabbit antibodies (Immunologic). Substrate was developed with DAB (DAKO). Imaging was performed using a Nikon Eclipse E800 microscope mounted with a Nikon digital camera DXM1200.

Model for the collective dynamics of MTs in pseudopods

Dynamics of MT bundles inside pseudopods was modeled using Monte Carlo simulations written in Matlab (version 2011b, Natick, MA, USA) similar to previous studies (Dogterom and Leibler, 1993; Janson et al., 2003; Laan et al., 2008). The total number of MTs N_{tot} was constant during each simulation, but varied from 3 to 10 for different conditions. MT growth and shrinkage were considered as deterministic processes with defined velocities, whereas catastrophe and rescue events of individual MTs were treated as random processes. The main parameters of dynamic instability were the growth V_{gr} and shrinkage V_{sh} rates, and the average catastrophe T_{gr} and rescue T_{sh} times. Growth rate and average catastrophe time for each

condition were obtained from the experimental measurements of the dynamics of EB3 comets inside pseudopods (Fig. 5G,H). For the shrinking rate and average rescue time we selected previously measured values of 20 μm/min and 0.14 min correspondingly (Kapoor and Panda, 2012). Each MT in the bundle started to grow at zero length in the "semi-infinite" geometry and switched between growing and shrinking phases. If the length of a MT was zero, it automatically switched to the growth phase. The final output of simulations was a set of MT lengths over discrete time sequences $L_i(t_j), i \in [1, N_{tot}], t_j = j \cdot dt, t \in [0, T]$, where dt is the time step and T is the total observation time. The length and growth velocity of the MT bundle were defined as the length and velocity of the longest MT in the bundle.

We assumed that the average catastrophe time depends linearly on the growth rate (Janson et al., 2003) and used the measured values of V_{gr} and T_{gr} far from the edge of the protrusion (in the absence of load, Fig. 5G,H) to calculate the corresponding coefficient of proportionality for each condition (Fig. S4B). MTs longer than the average MT length in the bundle were supposed to resist the compressive load (accounting for the round shape of the tip of protrusion), which led to a decrease of their growth rate. We assumed a simplified functional form for the force-velocity dependence $V_{gr}(f_{comp}) = V_{gr}(0)\exp\left(-\frac{f_{comp}}{f_{crit}N_{comp}}\right)$, where f_{comp} is the total compressive force generated at the edge of the pseudopod, N_{comp} is the total number of MTs sharing the load, $V_{gr}(0)$ is the growth rate far from the edge (in the absence of compressive force) and f_{crit} is characteristic "resistance force" of individual MT (Dogterom and Yurke, 1997). To estimate f_{crit} for each condition, we assumed that on average N_{tot}=5 and N_{comp} = 0.5*N_{tot} and that the total force f_{comp} experienced by the pseudopod is around 30 pN, i.e. on average each load-bearing MT experiences a force of 12 pN (Bornschlogl et al., 2013; Farrell et al., 2013; Koster et al., 2005; Pontes et al., 2011). Knowing characteristics of individual MT dynamics in the absence of force (f_{MT}=0, Fig.5G,H)

and under the estimated load (f_{MT}~12 pN, Fig.5N) allowed us to find the value of f_{crit} by fitting (Fig.S4C). As a result we obtained values of 37.7 pN for the control, 6.8 pN for the SLAIN2 siRNA and 7.4 pN for the CLASP1 siRNA conditions (Fig.S4C). These values are much higher than those measured previously *in vitro* (Dogterom and Yurke, 1997), which might hint at a more efficient force generation by MTs growing under *in vivo* conditions. However, the high f_{crit} value for the control condition might be an overestimate, since the number of microtubules sharing the load might be different for different conditions. Shrinkage was assumed to be force-independent.

All simulations were performed with the time step dt=0.1 s for the total time of T=20 min. To validate the model and map parameter space, we first performed simulations in the absence of the "compressed" state. In this case, the model becomes equivalent to the published earlier (Dogterom and Leibler, 1993). The simulation reproduced regimes of "unbounded" and "bounded" growth with a sharp transition taking place along the line L_{gr}=L_{sh}, where L_{gr}=$V_{gr}T_{gr}$ and L_{sh}=$V_{sh}T_{sh}$ (Fig. 7E, and see the purple line Fig.7F). For this reason, we chose these two combinations as the main parameters to build the system's parametric diagrams. For each simulation in the "unbounded" mode, we calculated the average pseudopod/bundle length at current time as $max(L_i(t_j))_i$ and fitted its time sequence with linear function to estimate the average velocity of pseudopod growth. With fixed value of L_{gr} the rate of pseudopod extension depended linearly on the value of L_{sh} (or vice versa), while moving deeper into the "unbounded" region of the parametric diagram, confirming the results obtained in (Dogterom and Leibler, 1993). After the introduction of a "compressed" state, the overall behavior of the model did not change. It showed regimes of "unbounded" and "bounded" growth and the same linear dependence of MT bundle/protrusion growth velocity on the main parameters. The main difference was that the position of the border separating two dynamic modes had changed. We calculated the new position of the separation

border on the parametric diagram numerically, using stochastic simulations of MT bundle described above. It is challenging to distinguish the difference between "bounded" and "unbounded" regimes in the area of parameters near the separation border due to highly stochastic behavior of the bundle (Fig. 7E). To avoid this ambiguity, we measured average protrusion/bundle growth velocity "deep" inside the "unbounded" growth area, where processive growth of the MT bundle is highly pronounced and its rate can be calculated precisely. We used five different values of L_{sh} (while keeping the L_{gr}, constant) and measured from the simulation the average bundle/protrusion velocity, which usually was in the range 1-10 μm/min. Since the growth rate of the MT bundle depends on the L_{sh} linearly, we were able to get the value of L_{sh}^{crit} located at the separation border between "bounded" and "unbounded" states (corresponding to the zero growth rate of the bundle) from a linear fit. This procedure was repeated five times and after averaging we got the value of L_{sh}^{crit} for the constant L_{gr} on the parametric diagram. The same search of L_{sh}^{crit} was repeated for the range of L_{gr} values, composing the final separation border between two regimes on parametric diagram.

As an independent verification of the model, we calculated the pseudopod extension rate at the point of the parametric diagram corresponding to the control condition. Simulations gave the value of 5.4 μm/min that is very close to the values of 3-6 μm/min observed in the experimental data.

Supplementary References

Akhmanova, A., Hoogenraad, C.C., Drabek, K., Stepanova, T., Dortland, B., Verkerk, T., Vermeulen, W., Burgering, B.M., De Zeeuw, C.I., Grosveld, F., and Galjart, N. (2001). Clasps are CLIP-115 and -170 associating proteins involved in the regional regulation of microtubule dynamics in motile fibroblasts. Cell *104*, 923-935.

Barde, I., Zanta-Boussif, M.A., Paisant, S., Leboeuf, M., Rameau, P., Delenda, C., and Danos, O. (2006). Efficient control of gene expression in the hematopoietic system using a single Tet-on inducible lentiviral vector. Mol Ther *13*, 382-390.

Bornschlogl, T., Romero, S., Vestergaard, C.L., Joanny, J.F., Van Nhieu, G.T., and Bassereau, P. (2013). Filopodial retraction force is generated by cortical actin dynamics and controlled by reversible tethering at the tip. Proc Natl Acad Sci USA *110*, 18928-18933.

Bouchet, B.P., Fauvet, F., Grelier, G., Galmarini, C.M., and Puisieux, A. (2011). p21(Cip1) regulates cell-substrate adhesion and interphase microtubule dynamics in untransformed human mammary epithelial cells. Eur J Cell Biol *90*, 631-641.

Dogterom, M., and Leibler, S. (1993). Physical aspects of the growth and regulation of microtubule structures. Phys Rev Lett *70*, 1347-1350.

Dogterom, M., and Yurke, B. (1997). Measurement of the force-velocity relation for growing microtubules. Science *278*, 856-860.

Ellis, A.L., Wang, Z., Yu, X., and Mertz, J.E. (2010). Either ZEB1 or ZEB2/SIP1 can play a central role in regulating the Epstein-Barr virus latent-lytic switch in a cell-type-specific manner. J Virol *84*, 6139-6152.

Farrell, B., Qian, F., Kolomeisky, A., Anvari, B., and Brownell, W.E. (2013). Measuring forces at the leading edge: a force assay for cell motility. Integr Biol (Camb) *5*, 204-214.

Fritz, R.D., Letzelter, M., Reimann, A., Martin, K., Fusco, L., Ritsma, L., Ponsioen, B., Fluri, E., Schulte-Merker, S., van Rheenen, J., and Pertz, O. (2013). A versatile toolkit to produce sensitive FRET biosensors to visualize signaling in time and space. Sci Signal *6*, rs12.

Grigoriev, I., Splinter, D., Keijzer, N., Wulf, P.S., Demmers, J., Ohtsuka, T., Modesti, M., Maly, I.V., Grosveld, F., Hoogenraad, C.C., and Akhmanova, A. (2007). Rab6 regulates transport and targeting of exocytotic carriers. Dev Cell *13*, 305-314.

Gutierrez-Caballero, C., Burgess, S.G., Bayliss, R., and Royle, S.J. (2015). TACC3-ch-TOG track the growing tips of microtubules independently of clathrin and Aurora-A phosphorylation. Biol Open *4*, 170-179.

Heck, J.N., Ponik, S.M., Garcia-Mendoza, M.G., Pehlke, C.A., Inman, D.R., Eliceiri, K.W., and Keely, P.J. (2012). Microtubules regulate GEF-H1 in response to extracellular matrix stiffness. Mol Biol Cell *23*, 2583-2592.

Honnappa, S., Gouveia, S.M., Weisbrich, A., Damberger, F.F., Bhavesh, N.S., Jawhari, H., Grigoriev, I., van Rijssel, F.J., Buey, R.M., Lawera, A., Jelesarov, I., Winkler, F.K., Wuthrich, K., Akhmanova, A., and Steinmetz, M.O. (2009). An EB1-binding motif acts as a microtubule tip localization signal. Cell *138*, 366-376.

Janson, M.E., de Dood, M.E., and Dogterom, M. (2003). Dynamic instability of microtubules is regulated by force. J Cell Biol *161*, 1029-1034.

Kapoor, S., and Panda, D. (2012). Kinetic stabilization of microtubule dynamics by indanocine perturbs EB1 localization, induces defects in cell polarity and inhibits migration of MDA-MB-231 cells. Biochem Pharmacol *83*, 1495-1506.

Koster, G., Cacciuto, A., Derenyi, I., Frenkel, D., and Dogterom, M. (2005). Force barriers for membrane tube formation. Phys Rev Lett *94*, 068101.

Koushik, S.V., Chen, H., Thaler, C., Puhl, H.L., 3rd, and Vogel, S.S. (2006). Cerulean, Venus, and VenusY67C FRET reference standards. Biophys J *91*, L99-L101.

Laan, L., Husson, J., Munteanu, E.L., Kerssemakers, J.W., and Dogterom, M. (2008). Force-generation and dynamic instability of microtubule bundles. Proc Natl Acad Sci USA *105*, 8920-8925.

Lansbergen, G., Grigoriev, I., Mimori-Kiyosue, Y., Ohtsuka, T., Higa, S., Kitajima, I., Demmers, J., Galjart, N., Houtsmuller, A.B., Grosveld, F., and Akhmanova, A. (2006). CLASPs attach microtubule plus ends to the cell cortex through a complex with LL5beta. Dev Cell *11*, 21-32.

Mimori-Kiyosue, Y., Grigoriev, I., Lansbergen, G., Sasaki, H., Matsui, C., Severin, F., Galjart, N., Grosveld, F., Vorobjev, I., Tsukita, S., and Akhmanova, A. (2005). CLASP1 and CLASP2 bind to EB1 and regulate microtubule plus-end dynamics at the cell cortex. J Cell Biol *168*, 141-153.

Moshfegh, Y., Bravo-Cordero, J.J., Miskolci, V., Condeelis, J., and Hodgson, L. (2014). A Trio-Rac1-Pak1 signalling axis drives invadopodia disassembly. Nat Cell Biol *16*, 574-586.

Pontes, B., Viana, N.B., Salgado, L.T., Farina, M., Moura Neto, V., and Nussenzveig, H.M. (2011). Cell cytoskeleton and tether extraction. Biophys J *101*, 43-52.

Riedl, J., Crevenna, A.H., Kessenbrock, K., Yu, J.H., Neukirchen, D., Bista, M., Bradke, F., Jenne, D., Holak, T.A., Werb, Z., Sixt, M., and Wedlich-Soldner, R. (2008). Lifeact: a versatile marker to visualize F-actin. Nat Methods *5*, 605-607.

Stepanova, T., Slemmer, J., Hoogenraad, C.C., Lansbergen, G., Dortland, B., De Zeeuw, C.I., Grosveld, F., van, C.G., Akhmanova, A., and Galjart, N. (2003). Visualization of microtubule growth in cultured neurons via the use of EB3-GFP (end-binding protein 3-green fluorescent protein). J Neurosci *23*, 2655-2664.

van der Vaart, B., Franker, M.A., Kuijpers, M., Hua, S., Bouchet, B.P., Jiang, K., Grigoriev, I., Hoogenraad, C.C., and Akhmanova, A. (2012). Microtubule plus-end tracking proteins SLAIN1/2 and ch-TOG promote axonal development. J Neurosci *32*, 14722-14728.

van der Vaart, B., Manatschal, C., Grigoriev, I., Olieric, V., Gouveia, S.M., Bjelic, S., Demmers, J., Vorobjev, I., Hoogenraad, C.C., Steinmetz, M.O., and Akhmanova, A. (2011). SLAIN2 links microtubule plus end-tracking proteins and controls microtubule growth in interphase. J Cell Biol *193*, 1083-1099.

Wolf, K., Te, L.M., Krause, M., Alexander, S., Te, R.J., Willis, A.L., Hoffman, R.M., Figdor, C.G., Weiss, S.J., and Friedl, P. (2013). Physical limits of cell migration: Control by ECM space and nuclear deformation and tuning by proteolysis and traction force. J Cell Biol *201*, 1069-1084.